

Stabilizing Sensorless Control Down to Zero Speed by Using the High-Frequency Current Amplitude

Thomas Szalai, Gotthard Berger, and Jürgen Petzoldt

Abstract—Sensorless control of permanent magnet synchronous machines (PMSM) down to zero speed using high-frequency (HF) signal injection is an established method. Stable operation during transient states still presents a challenge for this method, especially for motors with very small anisotropies. This paper introduces a new method for stabilizing the sensorless control scheme. It is shown that a misalignment between the estimated dq coordinate system and the actual rotor position causes a variation of the high-frequency current amplitude. Calculated values based on theoretical observation are compared to actual measurements of a hybrid stepper motor used as a PMSM. Several issues that can be used to determine if a motor is suitable for this approach are addressed. Finally, the effectiveness of the new control scheme is validated by implementation in the existing sensorless control of a hybrid stepper motor.

Index Terms—High-frequency (HF) signal injection, permanent magnet synchronous motor, sensorless control, signal processing.

I. INTRODUCTION

THE main advantages of sensorless control are reduced cost and increased reliability because the need for a mechanical sensor to measure the motor position and speed is eliminated. Using the speed-dependent back-EMF (see [1]–[3]), a very accurate and robust sensorless control can be implemented. Unfortunately, the back-EMF signal is too small to give reliable information about the rotor position at lower speeds. At standstill, there is no back-EMF and the method will fail.

Another group of techniques must be used to estimate the rotor position and velocity where back-EMF methods fail. These techniques (see [4]–[11]) inject a high-frequency (HF) voltage signal into the machine to track spatial saliencies. Using a wide variety of methods (see [10]–[14]), the resulting HF current is used to estimate the rotor position. Usually, the saturation saliency caused by the permanent magnets inside a permanent magnet synchronous machines (PMSM) and the constructive saliency oriented in the same direction are used to estimate the rotor position. In addition, most machines possess unwanted saliencies which distort the position signal and cause errors or a complete failure of the method. Because these saliencies are heavily dependent on motor geometry, a wide range of saliency

Manuscript received March 8, 2013; revised May 17, 2013 and July 11, 2013; accepted August 10, 2013. Date of current version February 18, 2014. Recommended for publication by Associate Editor R. Kennel.

The authors are with the Department of Power Electronics and Control, Ilmenau University of Technology, 98693 Ilmenau, Germany (e-mail: thomas.szalai@tu-ilmenau.de; gotthard.berger@tu-ilmenau.de; juergen.petzoldt@tu-ilmenau.de).

Digital Object Identifier 10.1109/TPEL.2013.2279405

TABLE I
PROPERTIES OF TESTED MACHINE AND CONVERTER

Parameter	Value	Unit
Name of Machine	21S31-0650-805L7-52(200)	-
Machine-Type	Hybrid-stepper-motor (2 phases)	
Nr. of pole pairs pp	50	-
Nominal Speed	1000	rpm
Nominal Torque	0,7	Nm
Nominal Current(rms)	2,8	A _{eff}
Resistance R _s	0,23	Ω
Inductance L _d (for I=0A)	0,78	mH
Inductance L _q (for I=0A)	0,80	mH
Permanent Flux Ψ _d	2,59	mVs
Converter-Type	Full Bridge Mosfet Switches	
DSP used for control	TMS320C2834x	
Switching Frequency	32768	Hz
DC-link voltage	40	V
Frequency of HF-signal	3276	Hz
Amplitude of HF-signal	10	V

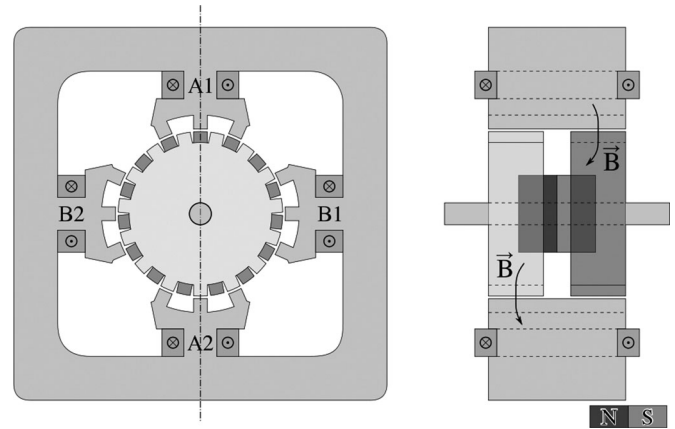


Fig. 1. Structure of HSM.

combinations has been found (see [13] and [15]–[17]). This paper analyzes the spatial saliency that can be found in every machine that is driven into partial saturation during operation. The problems and opportunities resulting from this saliency will be presented on the example of a small hybrid stepper motor (HSM), used as a PMSM. The parameters of the machine under test can be found in Table I, while Fig. 1 shows the general structure of an HSM. The only difference between the machine in Fig. 1 and the HSM under test is an increased number of pole pairs.

All tests were conducted using the standard converter provided by Jenaer Antriebstechnik GmbH, which controls each motor phase with a full bridge. No additional hardware has been used. Nonlinearities of the converter like dead time are not considered in this paper because the observed effects in the

TABLE II
SYMBOLS AND MEANINGS

Symbol	Meaning	Symbol	Meaning
\underline{u}^r	Voltage space phasor in rotor coordinates	i_{hp}^{hn}	HF-negative sequence current in HF-positive sequence coordinates
\underline{i}^r	Current space phasor in rotor coordinates	i_{hp}^{hn}	HF-negative sequence current in HF-negative sequence coordinates
\underline{u}^s	Voltage space phasor in stator coordinates	i_{hp}^{hp}	HF-positive sequence current in HF-positive sequence coordinates
\underline{i}^s	Current space phasor in stator coordinates	$ i_{hni} $	Amplitude of saliency i
R_s	Stator resistance	h_i	Harmonic number of saliency i
L_s	Tensor of stator inductance	i_{mag}	Imaginary magnetizing current equivalent to ψ_M/L
L_{qs}	Tensor of differential stator inductance	i_d	d-axis component of fundamental wave current
γ	Electrical angle	i_{hd}	d-axis component of high frequency current
$\dot{\gamma}/\omega$	Electrical angular velocity	i_q	q-axis component of fundamental wave current
ω_h	Angular velocity of HF-Signal	i_{hq}	q-axis component of high frequency current
ψ_M	Flux of permanent magnets	$\Delta L/\Delta i$	Slope of motor inductance
L_d, L_q	Inductance of d- and q-axis	L_{q0}	L_q at zero current
L_{od}, L_{sq}	Differential inductance of d- and q-axis	i_q'	Current component of estimated q-axis
L_{Min}	Minimum inductance along the circumference	φ_{cs}	Cross saturation angle
L_{Max}	Maximum inductance along the circumference	φ_{err}	Angle error between estimated and actual rotor position
$\Delta i_{hp} $	Difference between actual positive sequence amplitude and amplitude for $\varphi_{err} = 0$	φ_{corr}	Correction angle

experimental setup were at least a magnitude smaller than the effect of the analyzed spatial saliency. Likewise, nonlinearities resulting from the sampling process have been compensated to the best of the authors' knowledge and will not be analyzed separately. Both types of nonlinearities are known quantities and a number of compensation strategies can be found in [18]–[20].

II. PMSM WITH VARIABLE INDUCTANCE

A. HF Signal Injection

The injection of a rotating voltage space phasor as described in [4] was chosen as the basic HF technique to implement. The fundamental wave is modulated with an additional voltage space phasor rotating with a fixed frequency in the stator coordinate system. This generates a current space phasor rotating with the same frequency that consists of a positive sequence component and a negative sequence component due to the asymmetry of the motor. The HF current resulting from signal injection can be calculated using the voltage equation for PMSM in the rotor coordinate system

$$\underline{u}^r = R_s \underline{i}^r + L_s \frac{d\underline{i}^r}{dt} + j\dot{\gamma} L_s \underline{i}^r + j\dot{\gamma} \psi_M. \quad (1)$$

For HF signals, the voltage drop due to the stator resistance R_s can be neglected. The terms containing $\dot{\gamma}$ are also neglected due to the very low rotor speed. From the resulting HF model

$$\underline{u}_h^r = L_{\sigma s} \frac{d\underline{i}_h^r}{dt}, \quad L_{\sigma s} = \begin{bmatrix} L_{\sigma d} & 0 \\ 0 & L_{\sigma q} \end{bmatrix} \quad (2)$$

the HF-current in stator coordinates is calculated to

$$\begin{aligned} \underline{i}_h^s &= \frac{U_h}{2(\omega_h - \omega)L_{\sigma d}L_{\sigma q}} \left((L_{\sigma d} + L_{\sigma q}) e^{j(\omega_h t - \frac{\pi}{2})} \right. \\ &\quad \left. + (L_{\sigma d} - L_{\sigma q}) e^{j(2\omega t - \omega_h t - \frac{\pi}{2})} \right). \end{aligned} \quad (3)$$

The actual rotor position signals are contained in the negative sequence of the HF current, which is modulated by double rotor position ($2\omega t$). The position signals are extracted using the well-known bandpass–highpass combination [21], which can be seen

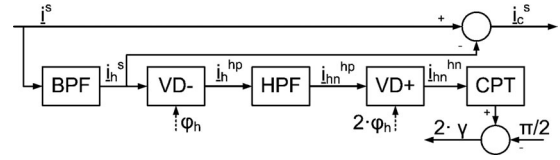


Fig. 2. Bandpass–highpass combination for extracting position signals from stator current with HF component.

in Fig. 2. After filtering out the fundamental wave current using the bandpass, the HF components are rotated into the HF positive sequence coordinate system, where a highpass is applied. At this point, only the negative sequence of the HF current remains

$$\underline{i}_{hp}^{hn} = \frac{U_h}{2(\omega_h - \omega)L_{\sigma d}L_{\sigma q}} \left((L_{\sigma q} - L_{\sigma d}) e^{j(2\omega t - 2\omega_h t + \frac{\pi}{2})} \right). \quad (4)$$

After one more transformation into the negative sequence coordinate system, the position signals needed for sensorless control are found

$$\underline{i}_{hn}^{hn} = \frac{U_h}{2(\omega_h - \omega)L_{\sigma d}L_{\sigma q}} \left((L_{\sigma q} - L_{\sigma d}) e^{j(2\omega t + \frac{\pi}{2})} \right). \quad (5)$$

B. Effects of Variable Inductance

In (1)–(5), the differential inductances $L_{\sigma q}$ and $L_{\sigma d}$ are assumed to be constant. This is not the case if additional saliences are present in the machine. This means (5) can contain additional terms as shown in (6), where $|i_{hni}|$ is the amplitude of the additional saliency i with the harmonic number h_i and the phase φ_i

$$\begin{aligned} \underline{i}_{hn}^{hn} &= \frac{U_h}{2(\omega_h - \omega)L_{\sigma d}L_{\sigma q}} \left((L_{\sigma q} - L_{\sigma d}) e^{j(2\omega t + \frac{\pi}{2})} \right) \\ &\quad + \sum |i_{hni}| \cdot e^{j(h_i \omega t + \varphi_i)}. \end{aligned} \quad (6)$$

The resulting distortion of the negative sequence HF current component \underline{i}_{hn}^{hn} will cause errors in the sensorless rotor angle. Nonetheless, (5) works very well as an approximation

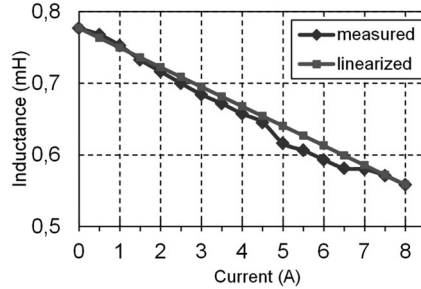


Fig. 3. Inductance reduction of the tested HSM along the rotor d -axis due to magnetic saturation resulting from injection of dc-current along the same axis.

for machines with sufficiently high saliency and low magnetic saturation, because the distortions are relatively small.

However, small positioning motors with rated power below 1 kW tend to operate with increased magnetic saturation, as the analyzed HSM clearly demonstrates (see Fig. 3). In this case, the interaction between the HF current and the saturation saliency will cause a significant signal distortion. Fig. 3 was obtained by injecting a dc current into one motor phase. The same phase was modulated with an additional HF voltage signal of the same frequency and amplitude as the one used in the sensorless control scheme. The inductance was then obtained by measuring the amplitude of the resulting HF current by solving the basic formula $\frac{|U|}{|i|} = |R + j\omega L|$ for the inductance L .

C. Mathematical Model

To calculate the distortion, it is necessary to introduce an HF motor model with variable inductances L_d, L_q . Neglecting EMF, it has the following form in stator coordinates:

$$u^s = R_s \dot{i}^s + \frac{d(L_s \dot{i}^s)}{dt}, \quad L_s = \begin{pmatrix} L_{\alpha\alpha} & L_{\alpha\beta} \\ L_{\beta\alpha} & L_{\beta\beta} \end{pmatrix}. \quad (7)$$

Usually, a sinusoidal inductance variation along the air gap and no additional spatial saliences are assumed in the literature as a valid approximation of the actual inductances. The inductance tensor for this approximation is

$$L_s = \begin{bmatrix} \frac{L_d + L_q}{2} + \frac{L_d - L_q}{2} \cos(2\gamma) & \frac{L_d - L_q}{2} \sin(2\gamma) \\ \frac{L_d - L_q}{2} \sin(2\gamma) & \frac{L_d + L_q}{2} - \frac{L_d - L_q}{2} \cos(2\gamma) \end{bmatrix}. \quad (8)$$

However, a motor model with variable inductance automatically implies the presence of cross saturation. That means L_d and L_q are not the actual minimum or maximum inductance inside the machine. The superposition between the magnetic field caused by the permanent magnets and the magnetic field caused by the current I_q will shift the magnetic axis towards the q -axis with increasing I_q . For motors with a high constructive saliency, the resulting shift of the area with the smallest inductance toward the q -axis will be negligible. On the other hand, the cross-saturation angle is almost identical to the angle shift of the magnetic field if saturation is the main component of the motor anisotropy. Fig. 4 compares the theoretical flux along both axes of the motor used in the experimental setup, if no constructive aspects are considered ($L_d = L_q$). The inter-

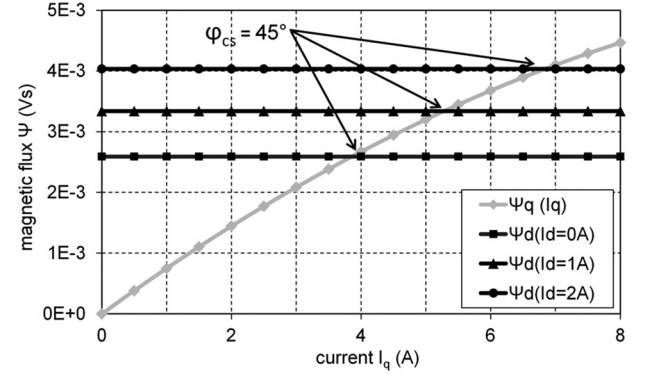


Fig. 4. Comparison between q -axis and d -axis flux for different I_q and $I_d = 0, 1, 2$ A.

section point of Ψ_d and Ψ_q is equivalent to a cross-saturation angle φ_{cs} of 45° ($\varphi_{cs} = \tan^{-1}(\Psi_q/\Psi_d)$). While this point can be shifted to higher I_q by increasing I_d (see curves for $I_d = 0, I_d = 1, I_d = 2$ in Fig. 4), the shift of the magnetic axis is still significant. Considering that L_d and L_q are almost identical for the tested machine, cross saturation plays an important role and should be considered when calculating the motor inductances.

Therefore, the inductances in the L_S -tensor are given as

$$L_{\alpha\alpha} = \frac{L_{\text{Min}} + L_{\text{Max}}}{2} + \frac{L_{\text{Min}} - L_{\text{Max}}}{2} \cos(2(\gamma + \varphi_{cs})) \quad (9)$$

$$L_{\beta\beta} = \frac{L_{\text{Min}} + L_{\text{Max}}}{2} - \frac{L_{\text{Min}} - L_{\text{Max}}}{2} \cos(2(\gamma + \varphi_{cs})) \quad (10)$$

$$L_{\alpha\beta} = L_{\beta\alpha} = \frac{L_{\text{Min}} - L_{\text{Max}}}{2} \sin(2(\gamma + \varphi_{cs})) \quad (11)$$

where γ is the actual rotor angle and φ_{cs} is the offset-angle caused by cross saturation. The minimum inductance is purely dependent on the amplitude of the applied current vector. Besides the fundamental wave components i_d, i_q and the HF components i_{hd}, i_{hq} , a magnetizing current i_{dmag} causing the same air gap flux as the permanent magnets is used as an equivalent for the calculation. Combined with the linearized inductance curve from Fig. 3, the minimum inductance is

$$L_{\text{Min}} = L_o - \frac{\Delta L}{\Delta i} \sqrt{(i_{\text{dmag}} + i_d + i_{hd})^2 + (i_q + i_{hq})^2}. \quad (12)$$

Equation (12) is a valid approximation for machines with small differences between L_d and L_q , as is the case with the tested HSM. For machines with highly different L_d and L_q , not only the amplitude but also the angle of the current space phasor will influence the resulting minimum inductance. Equation (12) is not applicable in this case. The maximum inductance is reached perpendicular to the magnetic axis, where the stator iron is not saturated. If the magnetic axis shifts, this unsaturated area shifts along with the magnetic axis. Assuming this unsaturated condition does not change when the magnetic axis shifts, the q -axis inductance for $i_q = 0$ represents the maximum inductance for all operating points of the motor

$$L_{\text{Max}} = L_{q0}. \quad (13)$$

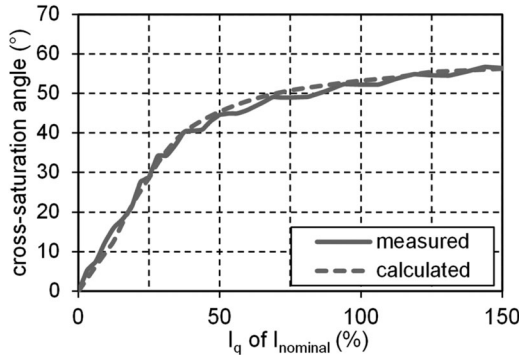


Fig. 5. Comparison between measured and calculated cross-saturation angle for the tested HSM from Jenaer Antriebstechnik GmbH.

Now that \$L_{\text{Min}}\$ and \$L_{\text{Max}}\$ are known, the cross-saturation angle \$\varphi_{cs}\$ is needed to solve (8)–(10). Usually, \$\varphi_{cs}\$ must be measured in every operating point of the machine. A simple lookup table is then used to correct the misalignment between the magnetic axis and the real rotor axis. In principle, the same can be done for a theoretical model. As was shown in [22], p. 132], an arctan function can be used to approximate the measured dependences. For the analyzed HSM, it was found that

$$\varphi_{cs} = k \cdot \tan^{-1} \left(\frac{L_{q0} - L_q}{L_{q0} - L_d} \right), \quad k = 0, 69 \quad (14)$$

is a very accurate approximation of the measured characteristic, as can be seen in Fig. 5. The cross saturation is normally measured during encoder operation by comparing the position signals produced by (5) to the actual rotor position given by the encoder for every current. In the experimental setup, the signal distortion due to unwanted saliences was too great for this method to produce accurate results. Instead, a direct Fourier transformation (DFT) for the +2 spatial harmonic was applied to the measured position signals to obtain the harmonic angle. The change of this angle with increasing \$i_q\$ corresponds to the cross-saturation angle displayed in Fig. 5. It is noteworthy that the cross-saturation angle \$45^\circ\$ is reached even earlier than estimated in Fig. 4. The most likely cause of this discrepancy are constructive aspects of the machine, which are not considered in Fig. 4.

With \$L_s\$ known, (6) can be solved for variable inductances and the resulting voltage equations for the \$\alpha\$- and \$\beta\$-components can be written as

$$u_\alpha = L_{\alpha\alpha} \dot{i}_\alpha + L_{\alpha\alpha} \dot{i}_\alpha + R i_\alpha + L_{\alpha\beta} i_\beta + L_{\alpha\beta} \dot{i}_\beta \quad (15)$$

$$u_\beta = L_{\beta\beta} \dot{i}_\beta + L_{\beta\beta} i_\beta + R i_\beta + L_{\alpha\beta} i_\alpha + L_{\alpha\beta} \dot{i}_\alpha \quad (16)$$

where the dotted factors \$\dot{x}\$ stand for \$dx/dt\$.

Because \$L_{\alpha\alpha}\$, \$L_{\beta\beta}\$, and \$L_{\alpha\beta}\$ are functions of \$i_\alpha\$ and \$i_\beta\$, (15) and (16) build a system of nonlinear differential equations. An analytic solution for this system is not feasible. Instead, (7)–(16) were used to simulate the saturation behavior of the machine for an approximate solution.

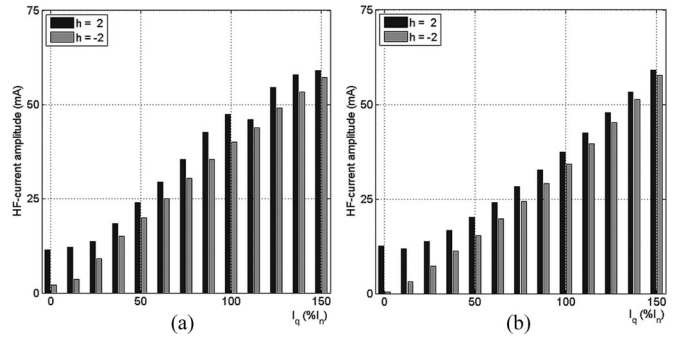


Fig. 6. Spatial saliences present in the negative sequence HF-current for (a) measurements on the hybrid stepper motor and (b) simulation of a PMSM with variable inductance for positive \$I_q\$ in the fundamental wave near zero speed (\$\omega = 6.28 \frac{1}{s}\$ during measurement).

D. Simulation

The simulation model was implemented in MATLAB-Simulink. Equation (1) was used to model the electrical part of the PMSM with the variable inductances obtained from (8)–(16). To replicate the influence of the current control loop, the complete algorithm for field-oriented control was implemented, and finally, the bandpass–highpass combination needed for extracting (6) from the machine current was built into the model. The motor angle needed for the control loop and the calculations of the electrical and saturation model was given as an external input. This is equivalent to a machine that is driven externally and ensures a constant motor speed for easier analysis.

Fig. 6(a) shows the measurements taken from the HSM during encoder operation. The second positive sequence spatial harmonic (\$h = 2\$) is the desired result of (5) and is used for sensorless control. The second negative sequence spatial harmonic (\$h = -2\$) represents the interaction of the HF current with the machine saturation. Simulating a PMSM with the machine parameters of the HSM used for experiments and applying a DFT with \$h = 2\$ and \$h = -2\$ to the extracted position signals (6) yielded the results shown in Fig. 6(b). The simulation results match the experiment closely. Because no constructive aspects were considered in the simulation, the implemented variable inductances must be the cause of the \$-2\$ spatial harmonic. Thus, the assumption, that the interaction between the HF current and machine saturation causes the position signal distortion, is validated.

III. SALIENCY MODEL

A. Implementation

It was found during the experiments that the presence of the \$-2\$ spatial harmonic causes the sensorless method to fail for \$I_q > 0.2I_n\$ if no further steps are taken to neutralize its effects. Currently, one of the most useful tools for enabling sensorless control despite the presence of unwanted saliences is the “Saliency Model” presented in [15]. The saliency model consists of a lookup table containing the expected position signals for every rotor angle. This includes the amplitude and phase

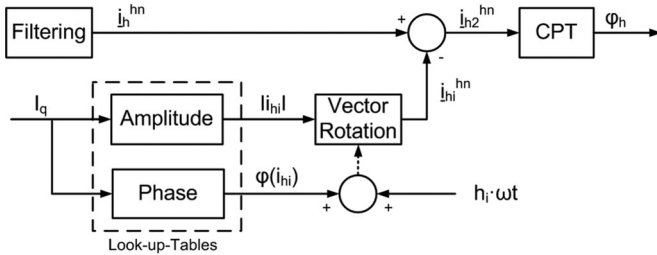


Fig. 7. Structure of the saliency model used to decouple unwanted saliences from the position signals.

for all saliences. In general, there are two ways to implement the saliency model. In the first case, the cross product between the actual positions signals and the signals obtained from the model, which contains all saliences of the motor, is used as an error signal to drive a tracking observer. In the second case, all unwanted saliences are decoupled from the combined position signals, leaving only the desired saliency information. This result is used to build a cross product with the signals obtained from a model containing only the tracked saliency to once again drive a tracking observer. Both methods are explained in detail in [15].

Tracking observers require information about the mechanical system and are very sensitive to parameter errors. Because of these disadvantages, a tracking observer was not realized in the experimental setup. Instead, the rotor angle is calculated directly from the position signals. This means that the first option could not be used. Accordingly, the decoupling saliency model was implemented as shown in Fig. 7. Amplitude and phase of the saliences to be decoupled are recorded during encoder operation of the machine and put inside the lookup table with orientation fixed to the coordinate system of the negative sequence HF current. A simple vector rotation fed with the phase from the lookup table and the harmonic of the rotor angle is used to generate the distortion components from the recorded amplitude. Once all unwanted saliences i are decoupled, the angle φ_h , which corresponds to the double rotor angle, can be extracted using Cartesian–polar transformation.

B. Experimental Results

With the described method, the undesirable saliency caused by the interaction between HF current and the machine saturation was decoupled from the sensorless position signals. The resulting position error of the sensorless model during encoder operation (see Fig. 8) is $\pm 5^\circ$. This error remains because, unlike the assumed model, the decoupled saliency is not a perfect sine wave. This accuracy is enough for stable sensorless control of most machines. Operating the HSM in sensorless mode reveals that this is not sufficient in our case (see Fig. 9).

There are four specific points during every machine revolution where the sensorless mode turns unstable. This periodic behavior is caused by the interaction between the desired +2 spatial harmonic and the unwanted -2 spatial harmonic contained within the HF negative sequence current. For easy demonstration of the underlying mechanism, it is assumed that the phases

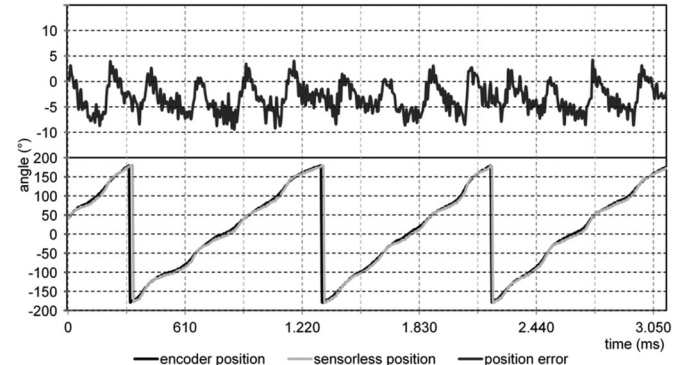


Fig. 8. Encoder position and corresponding sensorless position during *encoder operation* after compensation of unwanted anisotropy with a saliency model (bottom) and resulting position error of sensorless model (top) at nominal current(4 A).

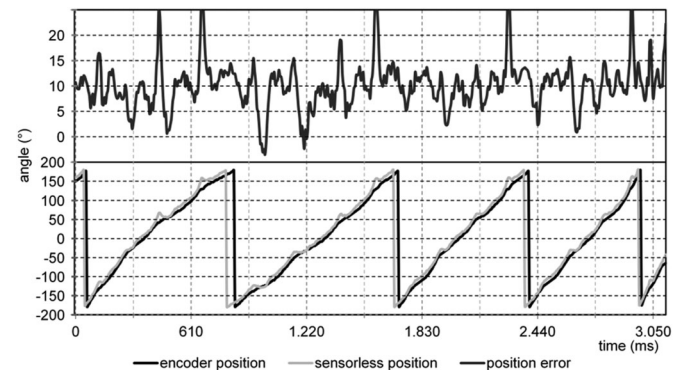


Fig. 9. Encoder position and corresponding sensorless position during *sensorless operation* after compensation of unwanted anisotropy with a saliency model (bottom) and resulting position error of sensorless model (top) at nominal current (4 A).

of both harmonics are zero; the combined position signal can be written as follows:

$$\underline{i}_{hn}^{hn} = |i_{-2}| \cdot e^{j(-2\omega t)} + |i_2| \cdot e^{j(2\omega t)}. \quad (17)$$

Using Euler's formula, (17) can split into complex components

$$\begin{aligned} \underline{i}_{hn}^{hn} &= \{|i_{-2}| \cdot \cos(-2\omega t) + |i_2| \cdot \cos(2\omega t)\} \\ &\quad + j \{ |i_{-2}| \cdot \sin(-2\omega t) + |i_2| \cdot \sin(2\omega t) \}. \end{aligned} \quad (18)$$

With the identities $\cos(-2\omega t) = \cos(2\omega t)$ and $\sin(-2\omega t) = -\sin(2\omega t)$, the amplitude of the overall signal is given as

$$\begin{aligned} |\underline{i}_{hn}^{hn}| &= \\ &\sqrt{\{(|i_2| + |i_{-2}|) \cdot \cos(2\omega t)\}^2 + \{(|i_2| - |i_{-2}|) \cdot \sin(2\omega t)\}^2}. \end{aligned} \quad (19)$$

Because the amplitudes $|i_2|$ and $|i_{-2}|$ are nearly identical (see Fig. 6), the term $\{(|i_2| - |i_{-2}|) \cdot \sin(2\omega t)\}^2$ is very small compared to the overall amplitude of $|\underline{i}_{hn}^{hn}|$ given in (19). As a consequence, the distorted position signals reach a maximum every time $|\cos(2\omega t)| = 1$, while a minimum is reached every

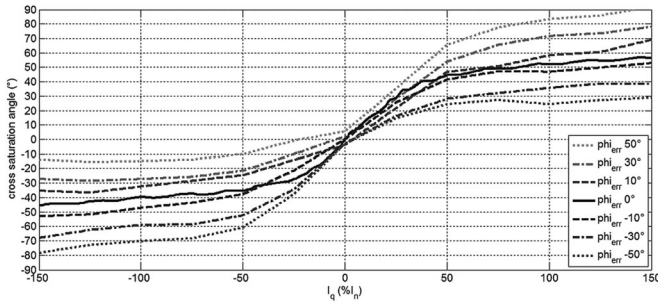


Fig. 10. Cross-saturation variation resulting from injecting current along the misaligned q -axis. Comparison between correct alignment ($\varphi_{err} = 0^\circ$) and different errors.

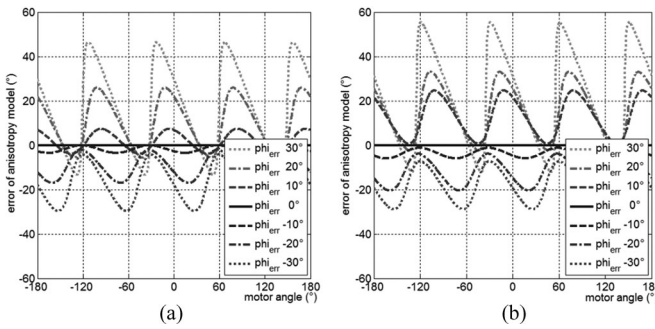


Fig. 11. Angle error caused by anisotropy model due to errors of the estimated rotor position for (a) 75% nominal current and (b) 150% nominal current.

time $|\cos(2\omega t)| = 0$. This happens four times in every electrical revolution and explains the four points of unstable operation observed during the experiments, which correspond to the minimum of the position signal amplitude. At these points, even a slight error in the saliency model will result in a significant angle error.

Operation at low speeds is still possible under these conditions, but the rotor angle is lost when the machine has to operate at standstill. The reason for this instability was found to be the very high saturation and cross saturation of the HSM. To show the effect of angle errors on cross saturation, the position signals of the HSM were measured for different i_q injected along a purposely misaligned q -axis and later analyzed with the DFT used in Sections I-C and I-D. As shown in Fig. 10, a slight angle error will shift the magnetic axis resulting in a faulty cross-saturation compensation. This, in turn, causes the saliency model to produce wrong compensation signals, making the error worse. The angle error caused by the anisotropy model for varying position errors ϕ_{err} is shown in Fig. 11 at 75% nominal current (a) and 150% nominal current (b).

In general, the model itself is stable if the resulting angle error is smaller than the position error φ_{err} , which caused the angle error in the first place. This is true for most operating points, but at the four critical points mentioned previously, this is not the case [see dotted lines in Fig. 11(b)]. Even without other errors present, the model will enter a positive feedback loop and turn unstable. Positive position errors cause a reduction of magnetic saturation because an unwanted negative direct current I_d is introduced. The amplitude of the actual position signals is

further reduced, resulting in a stronger instability when compared to negative position errors, which amplify the actual position signal. In accordance with this, the curves in Fig. 11 must be inverted for negative I_d .

While these findings can explain the unstable behavior of the sensorless control scheme, they cannot be used to stabilize the system. Cross saturation is an intrinsic part of the machine and cannot be “turned off.” At the same time, the saliency model is needed for the sensorless control to work. Other methods are needed to stabilize the system.

IV. HF AMPLITUDE CONTROLLER

A. Theory

The bandpass–highpass combination described in Section I can be used to extract the positive sequence of the HF current if the complete HF signal is rotated into the HF negative sequence coordinate system before the highpass is applied. Rotated back into the HF positive sequence coordinate system, this results in the following signal:

$$i_{hp}^{hp} = \frac{U_h}{2(\omega_h - \omega)L_{\sigma d}L_{\sigma q}} \left((L_{\sigma d} + L_{\sigma q}) e^{j(-\frac{\pi}{2})} \right). \quad (20)$$

As can be seen in (20), the positive sequence of the HF current does not contain information about the rotor position. It does, however, contain information about $L_{\sigma d}$ and $L_{\sigma q}$. As demonstrated in Sections II and III, both of these inductances are dependent on the currents i_d and i_q . This means a misalignment of the fundamental wave current will cause a change of $L_{\sigma d}$ and $L_{\sigma q}$, which can be measured using (20). The overall current of the fundamental wave will be split according to the misalignment φ_{err}

$$i_q = \cos(\varphi_{err}) \cdot i'_q, \quad i_d = \sin(\varphi_{err}) \cdot i'_q. \quad (21)$$

The linearized plot from Fig. 3 can be used to describe the current dependence of $L_{\sigma d}$ and $L_{\sigma q}$. For $L_{\sigma d}(i=0) = L_{\sigma q}(i=0)$, which is a valid approximation for motors with small differences between $L_{\sigma d}$ and $L_{\sigma q}$. This results in the following dependences:

$$L_{\sigma d} = L_{do} - \frac{\Delta L}{\Delta i} \cdot \sin(\varphi_{err}) \cdot i'_q \quad (22)$$

$$L_{\sigma q} = L_{qo} - \frac{\Delta L}{\Delta i} \cdot \cos(\varphi_{err}) \cdot i'_q. \quad (23)$$

After replacing the inductances in (20) with (22) and (23), a set of characteristic curves for the HF positive sequence amplitude as a function of i'_q and φ_{err} can be plotted. To keep the results comparable, the parameters from the experimental setup ($U_h = 10$ V, $\omega_h = 20584\frac{1}{s}$, and $\omega = 0\frac{1}{s}$) were used to generate Fig. 12. Obviously, the amplitude of the HF positive sequence barely changes due to position estimation errors as long as the amplitude of the fundamental wave i'_q stays relatively small [see 1A line in Fig. 12(a)]. On the other hand, the sensitivity of the amplitude to position errors grows with increasing i'_q . Accordingly, the slope of each characteristic line is used as a compensation coefficient C [see Fig. 12(b)] to calculate the

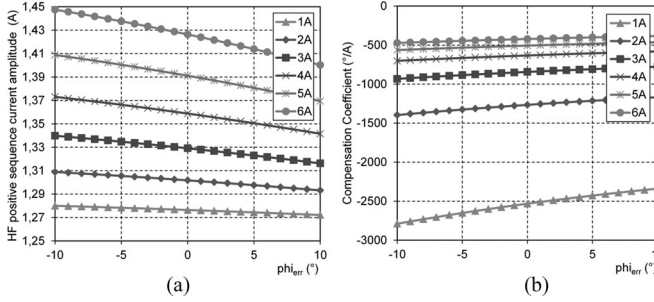


Fig. 12. Amplitude of the HF positive sequence current dependent on fundamental wave current i'_q and position error φ_{err} (a) and the resulting compensation coefficient for correcting the position error φ_{err} (b).

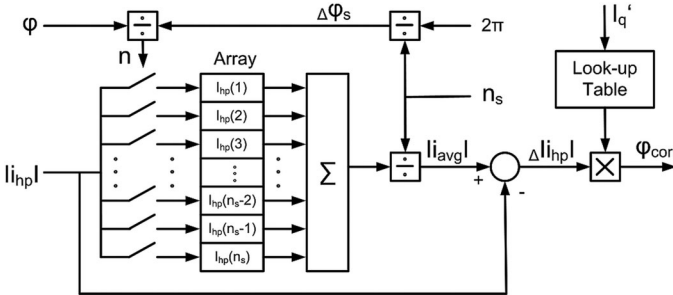


Fig. 13. HF amplitude controller used to control the HF positive sequence amplitude by correcting the position estimation error in the sensorless control scheme.

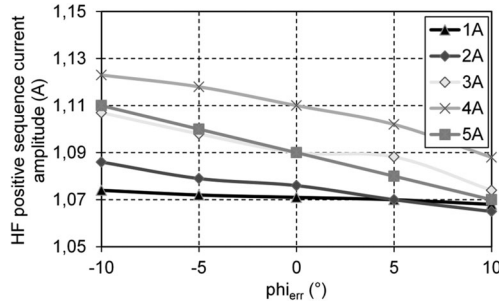


Fig. 14. Measurement of the relationship between the amplitude of the HF positive sequence current and the position estimation error

correction angle φ_{corr}

$$\varphi_{\text{corr}} = C \cdot \Delta |i_{hp}| \quad (24)$$

where $\Delta |i_{hp}|$ is the difference between the actual positive sequence amplitude and the expected amplitude for $\varphi_{\text{err}} = 0$.

B. Implementation

A comparative measurement on the experimental setup (see Fig. 14) clearly demonstrates that a direct implementation of the theoretical relationships in Fig. 12 is not possible. The rough tendency of the characteristic curves may be similar to the theoretical prediction, but neither the amplitude nor the arrangement of all curves compared to each other is consistent. The discrepancy in amplitude between theory and measurement can be traced to the fact, that (20) was extracted from the standard model, which does not take varying inductances into account.

The simulation of the model with variable inductances confirms this, although the exact mechanism behind this behavior is not yet understood. While it may be interesting, a closer look at this phenomenon will not help with solving the issue of implementation, because an additional external variable is interfering with the HF amplitude: The whole set of characteristic curves in Fig. 12(a) is a function of temperature, making it impossible to pinpoint an exact amplitude of the HF positive sequence for $\varphi_{\text{err}} = 0$, which is needed as a reference for (24).

Therefore, the challenge is to design a structure that correctly determines the amplitude for $\varphi_{\text{err}} = 0$ despite its dependence on temperature and the interaction with variable inductances. Once this hurdle is managed, (24) can be used to calculate the correction angle. This was done using the compensation coefficients in Fig. 12(b), because the slopes in Fig. 12(a) correlate very well with the measurements taken in Fig. 14.

To this end, an “HF amplitude controller,” as shown in Fig. 13, was implemented. It consists of a preprocessor for signal analysis and an adaptive proportional controller. The preprocessor uses the amplitude of the actual HF positive sequence current and the expected amplitude $|i_{avg}|$ for $\varphi_{\text{err}} = 0^\circ$ to generate the error signal $\Delta |i_{hp}|$. This error signal is then routed to the proportional controller whose adaptive signal gain is fitted to the fundamental wave using a lookup table generated from Fig. 12(b). The resulting output signal φ_{corr} is subtracted from the estimated rotor position angle to close the control loop.

The reference signal $|i_{avg}|$ is generated from measured motor data. To this end, the stator is split into sectors and each sector is assigned a cell inside the storage array. This cell gets overwritten with the actual HF positive sequence current amplitude as long as the rotor position is within the respective sector. If the rotor position is not within a sector, the assigned array cell will keep the last amplitude recorded before the sector was left. The average over all cells is finally used as the reference signal for the following proportional controller. Testing on the experimental setup revealed that the minimum number of sectors $n_s = 32$ should not be undercut to guarantee sufficient accuracy.

The proposed method for generating the reference signal works only if the average angle error over all sectors is close to zero. To fulfill this requirement, all array cells are overwritten with the value of the first active sector before the rotor starts moving. Due to the fact that the occurring angle errors for zero fundamental wave current are very small, this works very well for the purpose of initialization.

Fast current steps are another challenge the proposed HF-amplitude controller has to deal with. Due to the fact that array cells are only overwritten once the rotor enters their respective sectors, the PMSM must finish a full electrical turn before the correct reference $|i_{avg}|$ can be calculated for the changed current i_q . Depending on the step size, this will cause a short-lived imprecision of the estimated angle or cause the sensorless method to fail. To prevent this, the dynamics of the system must be limited through currents ramps or the values of all array cells must be corrected with the offset caused by changing the fundamental wave. The latter approach was chosen for implementation, because currents ramps would only work if the rotor is moving.

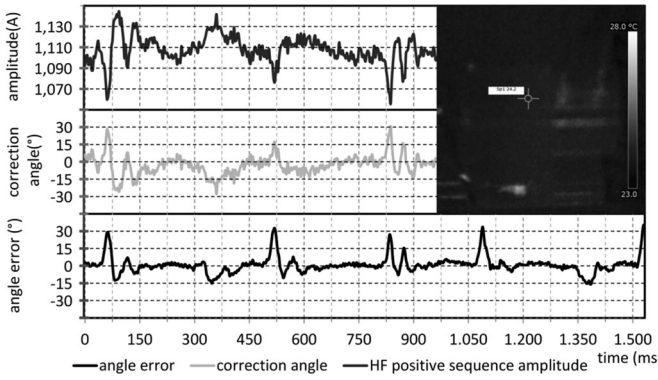


Fig. 15. HF positive sequence amplitude and correction produced by HF amplitude controller during open loop tests with cold motor (24°C).

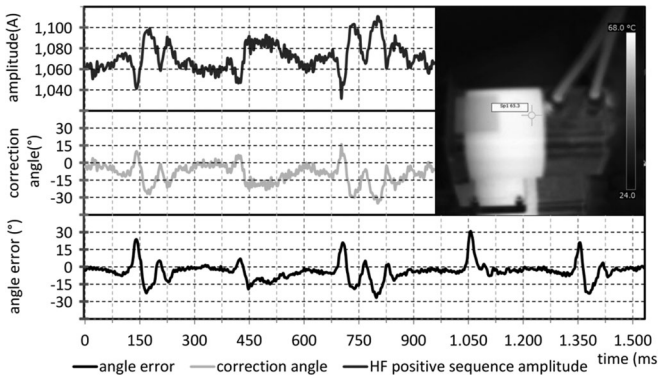


Fig. 16. HF positive sequence amplitude and correction produced by HF amplitude controller during open loop tests with hot motor (65°C).

To determine whether the temperature dependence of the HF positive sequence amplitude and the compensation coefficients is a problem, an open-loop test of the HF amplitude controller (the correction angle was calculated but not applied to the sensorless model) was done under cold and hot motor conditions. The results of the test at cold condition (current 4 A, sensorless control, cold motor at 24°C) are presented in Fig. 15. The uppermost graph of Fig. 15 shows that even smaller peaks of the angle error are seen in the amplitude of the HF positive sequence. The HF amplitude controller calculates the correction angle from these variations (middle graph). For the most part, the correction angle is almost identical to the angle error, but if the measurements taken from the amplitude are disturbed, the correction works only partially (see peak between 450 and 600 ms).

To test the motor under hot conditions, it was kept running until the surface temperature leveled out at 65°C . At this point, Fig. 16 was measured (current 4 A). The most notable difference compared to Fig. 15 is the overall reduction of the HF positive sequence amplitude. While a change of -30 to -40 mA does not sound much, this is in the same range as the amplitude variation caused by an angle error of 30° . Nevertheless, the correction angle produced by the HF amplitude controller still matches the actual angle error closely (compare middle graph and lowest graph). Two conclusions can be drawn from this: The continuously updated reference signal $|i_{\text{avg}}|$ corrects the –

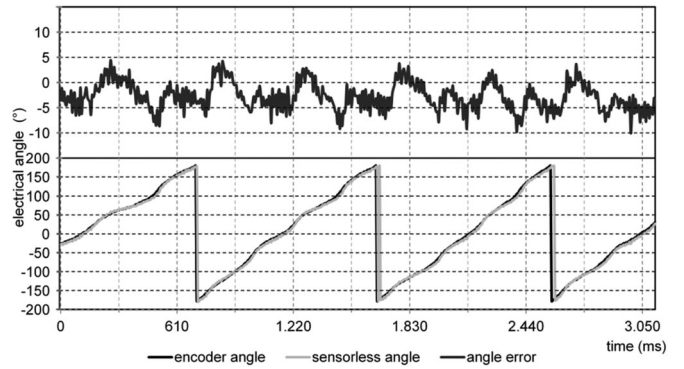


Fig. 17. Encoder position and corresponding sensorless position during *encoder operation* with active HF amplitude controller (bottom) and resulting position error of sensorless model (top) at nominal current (4 A).

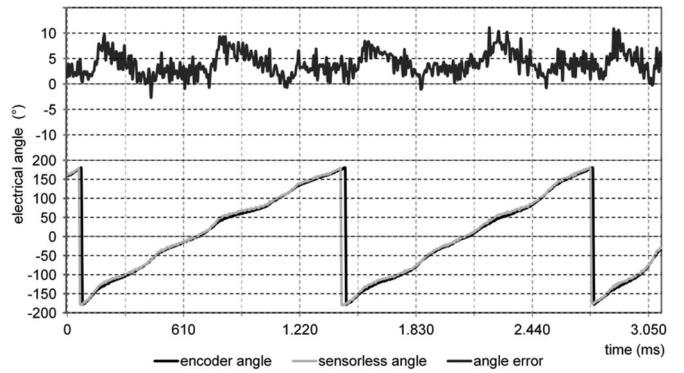


Fig. 18. Encoder position and corresponding sensorless position during *sensorless operation* with active HF amplitude controller (bottom) and resulting position error of sensorless model (top) at nominal current (4 A).

40 mA offset caused by the temperature rise as intended and the temperature dependence of the correction coefficients is small enough not to impede the performance of the HF amplitude controller.

C. Experimental Results—Static Behavior

The functionality validation of the implemented structure was done similarly to Section III. At first, the angle error of the sensorless model for nominal current during encoder operation was measured for several electrical rotations of the rotor. If the HF amplitude controller works properly, the results should closely match Fig. 8, because no interference is allowed while the estimated angle is correct. Comparing the measurement with an active HF amplitude controller (see Fig. 17) to the previous measurement from Fig. 8, there are almost no differences; the controller is idling.

Next, the control loop was switched to the sensorless control scheme with anisotropy model and HF amplitude controller. The upper part of Fig. 18 shows the corresponding estimation angle error at nominal current. The implemented structure performs its assigned task very good and stabilizes the sensorless control scheme. Except for a small change in offset, which will be explained further down, there is no difference regarding the estimated angle between sensorless operation and encoder operation. It is now possible to drive the PMSM with 150% nominal

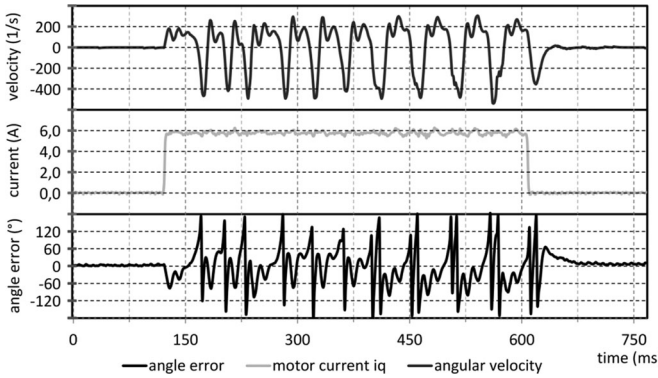


Fig. 19. Failure of sensorless control during torque step (150% I_n) without the proposed HF amplitude controller.

current at standstill even when staying at one of the previously unstable rotor positions.

A comparison of the estimation errors in Figs. 17 and 18 reveals that the error offset is changing from measurement to measurement. This variation is not caused by a faulty initialization or other hidden errors in the sensorless method. Measuring the estimation error for a full mechanical revolution shows that the offset is oscillating with the mechanical frequency. Most likely, the reference system is responsible. According to [23], the maximum angle error due to the eccentricity e of the code disc relative to the rotation center of the rotor shaft is given as

$$\Delta\varphi_m = \tan^{-1} \left(\frac{e}{r} \right) \quad (25)$$

where r is the radius of the code disc. The code disc of the experimental motor has a radius of 2 cm. For 50 pole pairs, the observed estimation angle variation of 10° results in a mechanical angle variation of $\Delta\varphi_m = 0.2^\circ$. When (25) is solved for e while using these parameters, the eccentricity of the code disc is $e = 70 \mu\text{m}$, which is a realistic value according to the manufacturer.

D. Experimental Results—Dynamic Behavior

Fast dynamic responses present a problem for sensorless control schemes. To demonstrate that the HF amplitude controller improves the stability of sensorless control during transients, the following test was done: The motor shaft was locked in place as well as the setup allowed. In practical terms, this means that the PMSM can turn almost a full electrical rotation before stopping, when 150% I_n is applied. This was done to ensure that the motor speed does not leave the working range of the sensorless scheme, which is stable up to 400 rad/s (electrical) during static operation. After this was done, a current step from 0 to 6 A (150% I_n) was applied, while the HF current controller was not active. As can be seen in Fig. 19, the sensorless control failed in this case. Shortly after the torque step is applied, the angle error starts jumping and the machine behavior becomes erratic, as is shown by the angular velocity calculated from the encoder position (uppermost graph).

For comparison, Fig. 20 was recorded with the HF amplitude controller active during the same test. While the angle error of

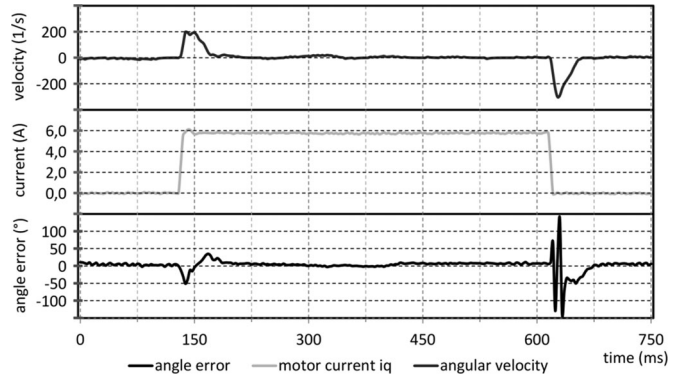


Fig. 20. Stable operation of sensorless control during torque step (150% I_n) after implementation of the HF amplitude controller.

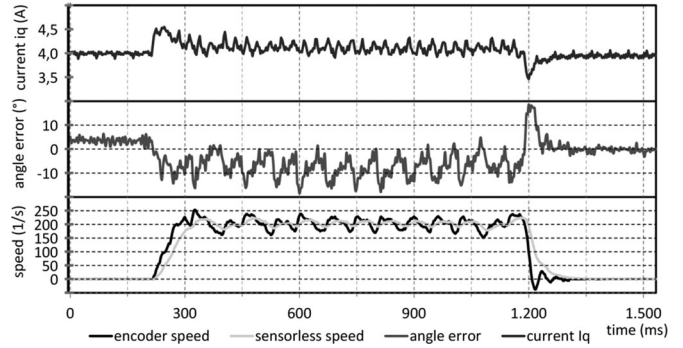


Fig. 21. Behavior of sensorless speed control during a reference speed step (electrical) from 0 to 200 rad/s and back while the HF amplitude controller is active.

the sensorless model is very high during the transients itself, the motor position is never fully lost and the control loop stabilizes the moment the transient is over. It is important to note that the cause of the angle error is not the current step itself, but the very fast change of the angular velocity. The PLL used for calculating the actual motor speed from the sensorless signals was designed with a time constant of about 10 ms to ensure smooth speed control even at very low speeds. The speed returned by the PLL is needed to correct the speed-dependent phase shift caused by the bandpass. This means a quick jump in motor speed results in an angle error due to the bandpass behavior, which is in turn increased because the compensation of unwanted saliencies does not work properly if the angle error is too high. The HF amplitude controller reduces these errors, allowing the machine to exceed the dynamic limitations given by the sensorless control scheme. It is by no means perfect because a significant angle error is present during the transient, but the overall motor position is not lost and precise positioning with increased dynamics becomes possible using this method.

For the second experiment, the motor under test was driven under speed control and an active load was applied to the motor during standstill using a dc machine. After this, the reference speed was changed to 200 rad/s for 1 s, after which the reference was set back to zero speed. The results of this test with enabled HF amplitude controller can be seen in Fig. 21. The applied active load was set to 100% of the nominal torque, as can be seen in

the uppermost graph. The angle error is very small at standstill. Once the speed reference is changed (time 200 ms in Fig. 21), the motor goes into overload for acceleration until the reference is reached. At this point the main problem of sensorless control can be seen once again: Compared to the actual speed, the PLL-calculated sensorless speed is delayed. A wrong speed results in wrong compensation angles for unwanted saliences and the bandpass phase shift—the angle error increases accordingly, as shown by the middle graph. The varying motor torque resulting from this, coupled with the active load, causes the motor speed to oscillate. Nonetheless, with the HF amplitude controller active, stable operation is possible. The same test was done without the HF amplitude controller active, but it was not possible to stabilize the control loop during standstill with an active load. Thus, a diagram showing a speed reference step cannot be provided at this point. This demonstrates clearly that the HF amplitude controller is also useful for compensating external disruptions to the system like those resulting from an active load.

V. CONCLUSION

Using the model of a PMSM with variable inductances, it has been validated that the -2 spatial harmonic present in the experimental setup is the result of interaction between the HF currents and the motor inductances. As such, every motor operating in saturation and high cross saturation will show this characteristic harmonic. A saliency model can be used to decouple this unwanted saliency, but due to the high cross saturation this is not enough to guarantee stable sensorless control. The HF positive sequence controller has been introduced to solve this problem. Using the normally unused positive sequence as reference, errors in the estimated angle can be detected and directly compensated. The stronger the inductances of a given motor change due to saturation, the higher the resolution of this technique. With the experimental setup presented in this paper, it allows for 150% load at standstill. A drawback of the HF amplitude controller is the necessity of additional measurements to extract the inductance current relationship displayed in Fig. 3. However, it may be possible to approximate this dependence during initialization of the sensorless control using (20). Research in this direction is still ongoing.

Another advantage of the proposed HF amplitude controller is the improved transient response. The dynamic constraints given by the sensorless control scheme using HF signal injection (time constant of PLL and bandpass) can be exceeded by means of the HF amplitude controller. While the HF positive sequence must be extracted using the same bandpass–highpass filter as for the position signals, no PLL is required to correct the phase shift of the filters. As a consequence, the dynamic limit of the HF amplitude controller is only dependent on the filter time constants, not on the PLL. Therefore, very accurate current sensing is required to reduce the filter time constants and to get closer to the theoretical dynamic limit given by the injection frequency. The comparatively high HF voltage amplitude of 10 V (25% of maximum value) was chosen to avoid the possibility of additional problems caused by insufficient accuracy of the current measurements. Tests with a smaller amplitude of 5 V

indicate that all presented structures work as intended at lower HF voltages, but further research is still required.

REFERENCES

- [1] S. Beineke, J. Schirmer, J. Lutz, H. Wertz, A. Bähr, and J. Kiel, “Implementation and applications of sensorless control for synchronous machines in industrial inverters,” in *Proc. 1st Symp. Sensorless Control Electr. Drives*, 2010, pp. 64–71.
- [2] J. Holtz, “Sensorless control of induction machine—With or without signal injection?” *IEEE Trans. Ind. Electron.*, vol. 53, no. 1, pp. 7–30, Feb. 2006.
- [3] L. Jarzewowicz, “Sensorless IPMSM drive with rotor position estimator based on analysis of phase current derivative,” in *Proc. IEEE Int. Symp. Ind. Electron.*, 2011, pp. 733–738.
- [4] N. Bianchi, S. Bolognani, J.-H. Jang, and S.-K. Sul, “Comparison of PM motor structures and sensorless control techniques for zero-speed rotor position detection,” in *Proc. Power Electron. Spec. Conference*, Jeju, Korea, 2006, pp. 1821–1827.
- [5] M. Schroedl, “Sensorless control of AC machines at low speed and standstill based on the ‘INFORM’ method,” in *Proc. Ind. Appl. Conf.*, 1996, pp. 270–277.
- [6] Y. Hua, M. Sumner, G. Asher, and Q. Gao, “Sensorless control for a PM machine with reduced current distortion using space vector PWM excitation,” in *Proc. 13th Eur. Conf. Power Electron. Appl.*, Barcelona, Spain, 2009, pp. 1–10.
- [7] R. Kennel, “Encoderless control of synchronous machine with permanent magnets—Impact of magnetic design,” in *Proc. 12th Int. Conf. Optim. Electr. Equipment*, 2010, pp. 19–24.
- [8] M. Linke, R. Kennel, and J. Holtz, “Sensorless position control of permanent magnet synchronous machines without limitation at zero speed,” 2002, pp. 674–679.
- [9] P. Giangrande and F. Cupertino, “A simplified position observer for zero-speed sensorless control of synchronous motors,” 2009, pp. 1014–1019.
- [10] F. Briz, A. Diez, and M. W. Degner, “Dynamic operation of carrier-signal-injection-based sensorless direct field-oriented ac-drives,” *IEEE Trans. Ind. Appl.*, vol. 36, no. 5, pp. 1360–1367, Oct. 2000.
- [11] M. Carpento, G. Maragliano, M. Marchesoni, and L. Vaccaro, “A new sensorless permanent magnet synchronous motor algorithm based on algebraic method,” in *Proc. 13th Eur. Conf. Power Electron. Appl.*, 2009, pp. 1–9.
- [12] I. Shinji, T. Mutuwo, D. Shinji, and O. Shigeru, “Sensorless control of permanent-magnet synchronous motors using online parameter identification based on system identification theory,” *IEEE Trans. Ind. Electron.*, vol. 53, no. 2, pp. 363–372, Apr. 2006.
- [13] R. Wrobel, A. S. Budden, D. Holliday, P. H. Mellor, and P. Sangha, “Design considerations for permanent magnet brushless machines for zero-speed sensorless position estimation,” in *Proc. 41st Ind. Appl. Conf.*, 2006, pp. 1494–1500.
- [14] H. D. Perassi, “Feldorientierte Regelung der permanenterregten Synchronmaschine ohne Lagegeber für den gesamten Drehzahlbereich bis zum Stillstand,” Ph.D. dissertation, Faculty Elec. Ing., Tech. Univ. Ilmenau, Germany, Dec. 2006.
- [15] M. W. Degner and R. D. Lorenz, “Using multiple saliencies for the estimation of flux, position, and velocity in AC machines,” *IEEE Trans. Ind. Appl.*, vol. 34, no. 5, pp. 1097–1104, Sep./Oct. 1998.
- [16] H. Kim and R. D. Lorenz, “Carrier signal injection based on sensorless control methods for IPM synchronous machine drives,” in *Proc. Conf. Rec. IEEE Ind. Appl. Conf.*, 2004, pp. 977–984.
- [17] A. S. Budden, R. Wrobel, D. Holliday, and P. H. Mellor, “Sensorless control of permanent magnet machine drives for aerospace applications,” in *Proc. Int. Conf. Power Electron. Drives Syst.*, 2005, pp. 372–377.
- [18] P. Aicher, “Winkelrekonstruktion und sensorlose Regelung von Hybridschrittmotoren,” Ph.D. dissertation, Faculty Mech. Eng., Tech. Univ. Munich, Munich, Germany, 2004.
- [19] R. Filka, G. M. Asher, P. Wheeler, and C. Silva, “Analysis of the influence of converter non-linearities on performance of sensorless controlled synchronous PM machine algorithms,” in *Proc. Eur. Conf. Power Electron. Appl.*, Toulouse, France, 2003, pp. 1–10.
- [20] K. Wiedmann, F. Wallrapp, and A. Mertens, “Analysis of inverter nonlinearity effects on sensorless control for permanent magnet machine drives based on high-frequency signal injection,” in *Proc. Eur. Conf. Power Electron. Appl.*, Barcelona, Spain, 2009, pp. 1–10.

- [21] C. S. Staines, C. Caruana, N. Teske, J. Cilia, and G. Asher, "Sensorless speed, position and torque control using AC machine saliencies," in *Proc. IEEE Int. Conf. Ind. Technol.*, 2004, pp. 466–473.
- [22] T. Frenzke, *Geberlose Drehmoment-Regelung für permanenterregte Synchronmaschinen in der Bahntraktion*. Erlangen, Germany: Shaker Verlag, 2007.
- [23] Thomas Samland, "Positions-Encoder mit replizierten und mittels diffraktiver optischer Elemente codierten Maßstäben", Ph.D. dissertation, Dept. Microsyst. Eng., Univ. Freiburg, Germany, 2011.
- [24] H. K. Khalil, *Nonlinear Systems*, 2nd ed. Englewood Cliffs, NJ, USA: Prentice-Hall, 1996.
- [25] J. Holtz and J. Quan, "Sensorless vector control of induction motors at very low speed using a nonlinear inverter model and parameter identification," *IEEE Trans. Ind. Appl.*, vol. 38, no. 4, pp. 1087–1095, Jul./Aug. 2002.

Authors' photographs and biographies not available at the time of publication.